Mechanism study of coupled aerodynamic and thermal effects using plasma actuation for anti-icing Ⓕ

ⓘD Xuanshi Meng, ⓘD Haiyang Hu, ⓘD Chang Li, et al.

COLLECTIONS

Ⓕ   This paper was selected as Featured

View Online   Export Citation   CrossMark

ARTICLES YOU MAY BE INTERESTED IN

Performance and mechanism analysis of nanosecond pulsed surface dielectric barrier discharge based plasma deicer
Physics of Fluids **31**, 091701 (2019); https://doi.org/10.1063/1.5115272

Passive feedback control of transonic buffet flow
Physics of Fluids **31**, 046103 (2019); https://doi.org/10.1063/1.5087014

Numerical investigation of control of dynamic stall over a NACA0015 airfoil using dielectric barrier discharge plasma actuators
Physics of Fluids **32**, 035103 (2020); https://doi.org/10.1063/1.5142465

Mechanism study of coupled aerodynamic and thermal effects using plasma actuation for anti-icing

Xuanshi Meng,[1,a] Haiyang Hu,[1,2] Chang Li,[1] Afaq Ahmed Abbasi,[1] Jinsheng Cai,[1] and Hui Hu[2]

AFFILIATIONS

[1] Department of Fluid Mechanics, Northwestern Polytechnical University, Xi'an 710072, China
[2] Department of Aerospace Engineering, Iowa State University, Ames, Iowa 50011, USA

[a] Electronic mail: mxsbear@nwpu.edu.cn

ABSTRACT

Anti-icing performance using the surface dielectric barrier discharge plasma actuator is studied using detailed visualization and surface thermal measurements. To reveal the physical mechanism of coupled aerodynamic and thermal effects on anti-icing, three types of actuators are designed and mounted on a NACA 0012 airfoil. The coupled aerodynamic and thermal effects are confirmed in still air. The results show that the plasma actuation is effective for in-flight anti-icing, and the anti-icing performance is directly related to the design of the plasma actuators based on the coupled aerodynamic and thermal effects. When the direction of plasma induced flow is consistent with the incoming flow, the heat generated by plasma discharge is concentrated in the region of the actuator and the ability of the actuator for heat transfer downstream is relatively weak during the anti-icing. When the induced flow is opposite to the incoming flow, there is less heat accumulation in the actuator region, while the ability of heat transfer downstream becomes stronger. With the consistent and opposite direction of induced flow, the plasma actuation can ensure that 57% and 81% chord of the lower surface of the airfoil are free of the ice accumulation, respectively. Another actuator is designed to induce the air jets approximately perpendicular to the airfoil surface. This exhibits both a stronger ability of heat accumulation locally and heat transfer downstream and hence ensures that there is no ice on the entire lower surface of the airfoil.

Published under license by AIP Publishing. https://doi.org/10.1063/1.5086884

I. INTRODUCTION

Ice accumulation can degrade the aerodynamic performance of an airplane significantly by decreasing lift while increasing drag. In wind energy, the ice accumulation on rotor blades has caused enormous overload threat on the tower, ice shedding hazard, and power generation losses. Prevention of ice accumulation on aerodynamic components has been a topic of great concern in the industry.[1-5]

The current anti-/de-icing methods fall into two distinct categories: (1) anti-icing (i.e., ice prevention) and (2) de-icing (i.e., ice removal). The methods can also be classified into three categories:[6,7] (1) the liquid-based, such as weeping wings, (2) the mechanical-based, such as pneumatic boots,

and (3) thermal-based, such as hot-air[8] and electro-thermal systems.[6]

The breakthrough of the significant technology in the area of aerodynamics, materials, and power raised many challenges on the current anti/de-icing methods. For example, the application of natural laminar flow technique requires the extremely smooth and precisely finished surfaces, while the current mechanical-based and hot-air anti/de-icing techniques have surface gaps and steps configurations which can provoke laminar-turbulent transition.[9] Moreover, recently various mathematical and numerical models have been proposed to simulate the ice accretion over the three dimensional surfaces and rotors[10,11] to help in development of novel icing control methods.

Another example, the bleed hot air system is the method mostly used by jet aircraft to keep flight surfaces above the freezing temperature required for ice to accumulate. But this system will not be suitable for the next generation aviation as aviation is advancing toward the all-electric and composite materials aircraft technologies. As there is no hot air system for an all-electric aircraft, the hot air system is not beneficial for the protection of composite structures because of the material's temperature limitations.[12–14] Therefore, the novel methods and techniques for more efficient anti/de-icing performance are considered desirable.[15–17]

Plasma flow control has received growing research attention as an active flow control technique. One such development is the use of surface dielectric barrier discharge (SDBD) plasma actuators driven by an alternating current (AC) source for active flow control. The AC-SDBD plasma actuator is composed of two electrodes separated by a dielectric material arranged in an asymmetric fashion. Application of a sufficiently high-voltage AC signal between the electrodes weakly ionizes the air over the dielectric covering the encapsulated electrode. The ionization of the air is a dynamic process within the AC cycle. The ionized air, in the presence of the electric field, results in a body force vector that acts on the ambient air and therefore induces a velocity field. Such induced airflow can be modulated to achieve active aerodynamic control.[18–24] It has the advantages of non-mechanical parts, zero reaction time, broad frequency bandwidths, and relatively low energy consumption. Most importantly, the plasma actuators can be conveniently arranged on the surface of the vehicle parts or the wind turbine.

The drawback of plasma flow control is its low efficiency of energy conversion (the surface discharge-induced kinetic efficiency versus discharge current is only several percents).[18] For an AC-SDBD plasma actuator, the large part of the electrical power is transferred into heat energy, and thus it also has an obvious thermal effect on the electrode sheet, the substrate, and the surrounding air during the high-voltage discharge besides the aerodynamic effect.[25] The thermal behavior of AC-SDBD has been observed in previous studies.[26–32]

Joussot et al.[28] studied the dielectric temperature characteristics of AC-SDBD plasma by infrared thermography in both quiescent air and wind tunnel. They have found the turbulent boundary layer has a higher convection heat dissipation capability than the laminar boundary layer. Erfani et al.[29] revealed that the maximum velocity produced by the actuator depends directly on the dielectric surface temperature. Rakshit et al.[30] concluded that the temperature distribution of the major part of the dielectric surface is determined by the convection of gas above the surface. Direct heat transfer at the plasma generated region plays only a minor role. Fredrico et al.[31] experimentally studied the total heat dissipation of AC-SDBD. They found the main dissipative region of thermal energy is in the plasma region. For voltages above the breakdown voltage, gas heating accounts for the majority of the thermal energy generated by the actuator.

To further increase the efficiency and broaden the area for SDBD plasma actuators, Meng et al.[33] proposed a

concept of plasma icing control by utilization of both aerodynamic and thermal effect. The concept is to achieve the flow control and icing control using the same set of equipment, i.e., plasma actuators. The actuators are used for icing control in icing conditions and for flow control in non-icing environments. Plasma icing control technology almost satisfies all the icing control requirement of the next generation aircraft. First, it can make use of both the aerodynamic and thermal effects of the plasma that means it can utilize most of the power consumption of the plasma actuation. Second, it can be smoothly set on any surface, i.e., the parts of aircraft, to keep the natural laminar flow. Third, the temperature of the AC-SDBD discharge has a limited temperature increase due to its stable self-limiting character in atmospheric pressure, so it will protect the composite structures during anti-/de-icing. Finally, it is can be easily settled on all-electric aircraft as a full electric-based icing control technique.

Experimental studies by Cai et al.[34,35] showed the feasibility of plasma icing control on a cylinder model. The anti-/de-icing performance of the AC-SDBD plasma actuator is evaluated based on visualization and thermal measurement in the icing wind tunnel. Results showed that the mixed ice layer can be completely removed from the cylinder surface after a few minutes of plasma actuation in the deicing test. In the anti-icing test, plasma actuation can completely prevent ice formation on the surface of the cylinder model. Pouryoussefi et al.[36] studied the effects of plasma on the separation of bubbles formed by ice formation for angles of attack close to stall and post-stall. The results concluded that actuators are able to eliminate the adverse effects of icing on the model by controlling the separation bubble. Zhou et al.[37] performed the study over an airfoil model using the SDBD plasma actuator for icing mitigation. The results demonstrated that the actuators can be used as a promising anti-icing tool for aircraft icing mitigation by taking advantage of the thermal effects of plasma actuation, and the induced aerodynamic effect of the actuator has not been discussed in that study. Tian et al.[38] showed an effective icing control using a pulsed dielectric barrier discharge plasma actuation with a freestream velocity of 90 m/s, which exhibits high possibility of the real application of SDBD plasma actuation in preventing aircraft icing in flight.

The purpose of this research is to reveal the physical mechanism of coupled aerodynamic and thermal effects on anti-icing and then provide a criterion for plasma actuator optimization. Three different types of actuators are designed to generate the induced airflow in different directions to the incoming flow. Two sets of plasma actuators are placed on the same surface of the airfoil, and the anti-icing effects of the plasma are observed by comparing each set. One set of actuators is turned off, while the other is on during both quiescent air and wind tunnel tests. The actuators are characterized using the two-dimensional Particle-Image-Velocimetry (2D-PIV) technique and the surface temperature distribution measurements. The plasma icing control over the airfoil is studied in an icing wind tunnel; discussion and conclusion are drawn based on experimental results in the quiescent air and wind tunnel.
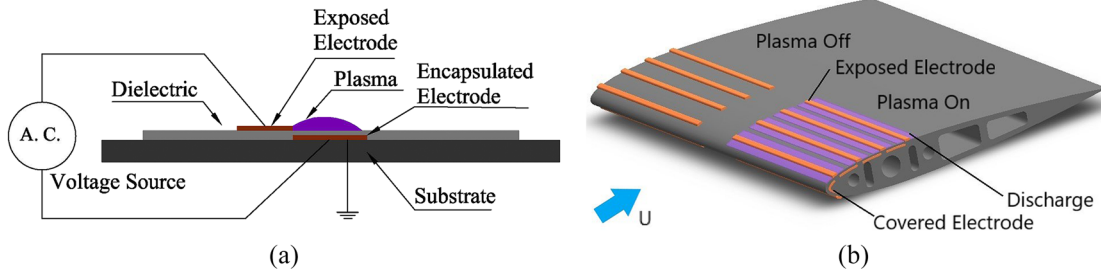
FIG. 1. Schematic illustration of airfoil model and plasma actuators. (a) Single SDBD plasma actuator. (b) Actuators mounted on airfoil model.

II. EXPERIMENTAL SETUP

A. Wind tunnel facility and airfoil model

Anti-icing experiments are conducted in a closed-circuit low-speed icing wind tunnel. The icing wind tunnel can simulate the super-cooled droplets icing environment and study the influence of ice on airframes or aero propulsion systems. The test section is 2.0 m long with 0.4 m (height) × 0.4 m (width) in cross section and four optically transparent side walls. In the present study, the freestream velocity and the static air temperature are kept constant at U_∞ = 40 m/s and T_∞ = −5 °C, respectively. The liquid water content (LWC) level of the incoming airflow is 1.0 g/m^3. The varying water droplet size range has an effect on aircraft icing.[39] In the present study, the size range of super-cooled water droplets is about 10-100 μm. The angle of attack (AOA) is fixed at 5° at all the test cases. Only the icing control over the leading edge and the lower surface is studied due to the less ice accumulation over the upper surface and the limitation of the experimental setup.

For all the test cases, the icing-wind-tunnel is operated at a prescribed frozen-cold temperature level for about 20 min to ensure that the test section reaches a thermal steady state. Then, the SDBD plasma actuator is switched on for about 80 s (determined by the operation time of the plasma source) before turning on the water spray system. The time is set at the beginning of the water spray. As the water spray system is switched on, the super-cooled water droplets carried by the incoming airflow would impinge onto the surface of the airfoil model to start the ice accumulation process.

The test model used in the experiments is the NACA 0012 airfoil. The chord of the airfoil is 0.15 m, and the span is 0.4 m, which is the same as the width of the icing-wind-tunnel cross section. The corresponding Re number is about 3.6×10^5 based on the chord of the airfoil in the airflow without water spray. The model is made of a hard plastic material and manufactured using a three-dimensionally printed technique that built the model layer-by-layer with a resolution of about 25 μm. The surface of the model is finished with a coating of primer and wet-sanded to a smooth finish using 1000 grit sandpaper.

B. Plasma actuators

A multi-SDBD actuator, i.e., the actuator includes a few long strips of single SDBD plasma-actuators, is installed on the lower surface of the airfoil. One single SDBD actuator is composed of two 0.07-mm-thick copper electrodes separated by Kapton tape dielectric arranged in an asymmetric fashion. The dielectric barrier is composed of 3 layers of 0.13-mm-thick Kapton tape; see Fig. 1(a). There is no gap or overlap between the exposed and encapsulated electrodes to encourage uniform plasma generation. The design of the single actuator is optimized for high induced flow velocity, large range of influence, and low power consumption.

Two sets of the multi-SDBD plasma actuator are attached on the lower surface of the airfoil in Fig. 1(b). Each set of plasma actuators is arranged symmetrically to the middle span of the airfoil model. The starboard-side actuator is kept off, while the port-side actuator is turned on during the anti-icing experiment. The ice accumulation process over the airfoil surface for the plasma-on side (i.e., port side) would be compared side-by-side against that of the plasma-off side (i.e., starboard side) in order to evaluate the effectiveness of the SDBD plasma actuator under the identical icing conditions.

Figure 2 shows the configurations of three types of actuators. Experiments are performed three times for three types of SDBD actuators. Figure 2 shows the schematics of three types (Type-1, Type-2, and Type-3) of actuator layouts tested
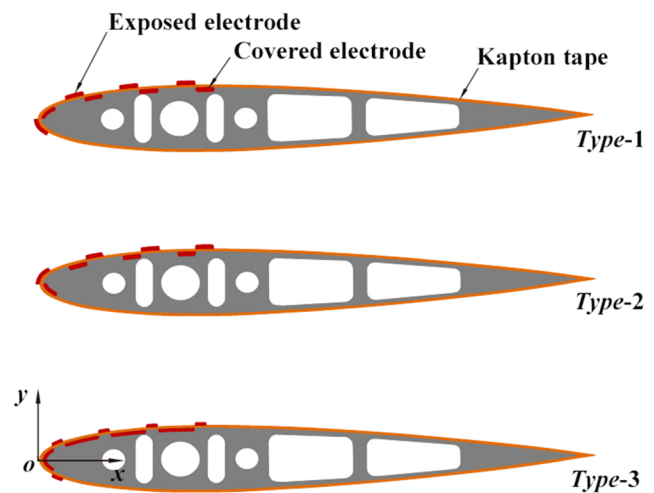

FIG. 2. Designs of three type actuators.

in three time periods. For the actuators, the effective spanwise length is about 96 mm and chordwise is about 50 mm. The first two types of actuators (*Type*-1 and *Type*-2) consist of 4 exposed electrodes (5 mm wide, chordwise) and 4 buried electrodes (5 mm wide), while 5 exposed electrodes (3 mm wide) and 4 covered electrodes (5 mm wide of the first one, 10 mm wide of the rest) are presented for the *Type*-3 arrangement. The *Type*-1 actuator is designed to generate an induced flow in the same direction as of the incoming flow, and the *Type*-2 actuator is used to generate an induced flow in opposite to the incoming flow, while the *Type*-3 actuator can generate the induced jets in vertical directions.

The actuator is connected to a high-voltage AC source that can provide a peak-to-peak amplitude varying from 0 to 30 kV and center frequency from 1 to 100 kHz. The voltage applied to the actuator is measured by a Tektronix P6015A high-voltage probe. The current through the actuator is measured by a high response AC current probe, Model Pearson 2877 of Pearson Electronics Inc. The signals from these devices are processed in real time by a Tektronix DPO3054 oscilloscope.

C. Flow diagnostics

A high-speed imaging system, Model Dimax of PCO-Tech, Inc., with 2000 pixels × 2000 pixels maximum spatial resolution, along with a 60 mm optical lens (Nikon, 60 mm Nikkor 2.8D) is used to record the ice accumulation process. The high-speed imaging system is mounted above the airfoil model with a measurement window size of 210 mm × 210 mm (i.e., with a spatial resolution of 9.5 pixels/mm) to record the ice accumulation process over both the plasma-on and plasma-off sides of the airfoil surfaces simultaneously.

An infrared (IR) thermal imaging system, Model FLIR-A615, is used to map the corresponding temperature distributions over the surface of the airfoil model during the ice accumulation process simultaneously. For acquiring the IR thermal images, an infrared emission transmissible window is embedded on the top plate of the test section. The IR thermal imaging system is focused on the front portion (i.e., the region near the airfoil leading edge) of the airfoil model with a measurement window size of 110 mm × 90 mm, which is indicated by a rectangular window with the dotted red line in Fig. 3. As a result, the spatial resolution of the IR thermal images is 5.3 pixels/mm.

The SDBD plasma actuators had been characterized in the still air before conducting the ice accumulation experiments in the icing-wind-tunnel. The induced flow fields are quantified by the two-dimensional particle-image-velocimetry (2D-PIV) technique. The surface temperature distributions are measured by a thermal camera.

The PIV images are acquired and processed using a PIV system from Dantec Dynamics. The flow seeds are the smoke particles of approximately 1 μm in diameter commonly used in the cinema industry. One Nd:YAG 200-mJ laser system is used in conjunction with spherical and cylindrical lenses to form a thin light sheet that allows PIV measurements at a maximum repetition rate of 15 Hz. The time interval between laser pulses used for particle scattering is 1 ms which is tuned according to
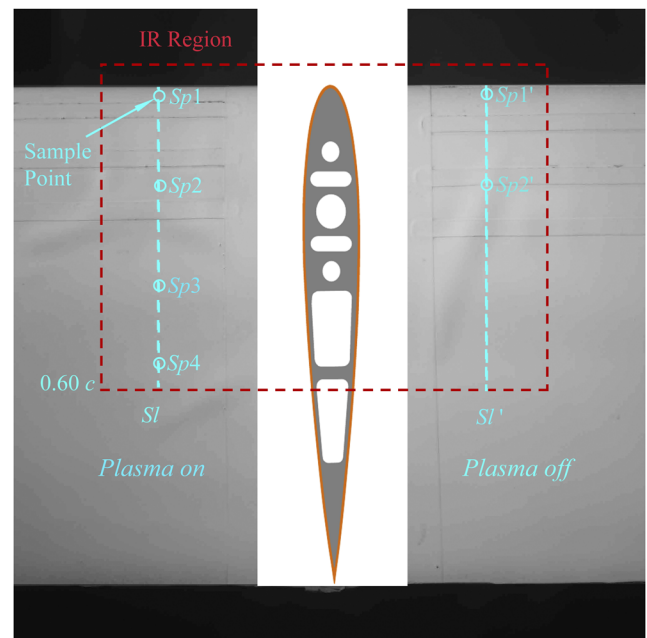

FIG. 3. Schematic illustration of sample lines and points.

the flow velocity, camera magnification, and correlation window size. A CCD camera of 1200 pixels × 1600 pixels is used to record the cross-flow image with 205 mm × 153 mm real size. DynamicStudio Stereo PIV software is used to process the image pairs and compute the time-averaged velocity fields. Data are processed in 32 pixels × 32 pixels interrogation areas with 50% overlap. Data for the plasma actuator in the still air are acquired with the camera perpendicular to the light sheet.

Surface temperature measurements in the still air are obtained with a FLIR Systems T660 infrared (IR) camera in the 7.5-14 μm spectral range with a sensitivity of within 0.02 °C at room temperature of 25.7 °C. The highest accuracy for T660 is ±1% of the reading. The camera has a resolution of 640 × 480 pixels. The working distance of the camera is 500 mm with a 400 mm × 30 mm field of view. The camera recorded the infrared emission of the dielectric surface which is a function of its temperature. For each case studied, the actuator is not activated for initial 2 s and then turned on for 35 s. The surface emissivity of the Kapton is used to calculate the temperature, which is set at 0.83.[40] The surface temperature of the exposed electrode, made of copper, is not given in this study due to the different surface emissivity. Other parameters, including the working distance of the camera, the room temperature, and its relative humidity, are also taken into account for the temperature calculation.

In order to compare the different ice accumulation process between plasma-off and plasma-on, two sample lines, S*l* and S*l′*, are selected and located in the plasma-on and plasma-off regions, respectively. The sample points, S*p*1-S*p*4 and S*p*1′-S*p*2′, are chosen and located at 2%, 20%, 40%, and

55% chord, respectively, to study the chordwise temperature distributions.

III. ACTUATOR CHARACTERIZATION

For 2D-PIV tests, the geometric parameters and the mounting positions of the plasma actuator on the airfoil are kept the same as those used in the wind tunnel tests. The peak-to-peak voltage and frequency are 14 kV and 10 kHz, respectively, which are also the same as those of the wind tunnel test. Two hundred instantaneous image pairs are processed by the time-averaged method to obtain the averaged velocity fields of the different actuators. Figure 4 shows the contours of time-averaged velocity and vorticity for three different types of actuators, and the velocity vectors are plotted over the contours. The spanwise vorticity ω_z is calculated based on the velocity measurements.

Under the same peak-to-peak voltage and frequency, obvious differences were observed in the induced flow field of three different types of actuators. Within the observed flow field, it is shown that the *Type*-1 actuator produces a locally tangential blowing close to the surface of the airfoil. The obtained maximum induced velocity is about 2 m/s. The induced flow field ranges at approximate x/c = 0.1–0.7 along the chord with a height of about $0.01c$ from the surface. The flow field is not that smooth above the single SDBD electrode because of the local air acceleration. The corresponding range of the vorticity is about [−500, 1100] s^{-1}. It can be seen

that the AC-SDBD actuator imparts momentum to the flow, much like flow suction or blowing but without mass injection. It has an apparent effect on the boundary layer velocity profile.[41-43]

The *Type*-2 actuator generates a locally tangential blowing, opposite to *Type*-1, to the leading edge of the airfoil. The induced flow crosses the leading edge via an apparent Coanda effect. The obtained maximum induced velocity is about 3.7 m/s. The induced flow field ranges at approximate x/c = −0.1–0.3, and the range of the corresponding vorticity is about [−2600, 1000] s^{-1}. The height of the induced flow fields is about $0.15c$ from the surface, which is 1.5 times that of the *Type*-1 actuator.

For the *Type*-3 actuator, it produces an induced airflow at the leading edge of the airfoil that is approximately perpendicular to the local surface. The height of the induced flow exceeds the measured region. The obtained maximum induced velocity is about 2.7 m/s. The range of the corresponding vorticity is about [−1600, 1400] s^{-1}. It can be seen that the *Type*-3 actuator produces higher vorticity due to the mutual influence of multiple induced flows.

Figure 5 shows the contours of surface temperature (left) at t = 80 s time delay for different actuators. The sample lines along the chordwise and spanwise are indicated by blue dashed lines. The intersection of the sample lines is set as the sample point. The temperature along the spanwise at the sample line for 80 s time delay is also shown in Fig. 5 (right). Since the long strip actuator is used, the theoretical temperature
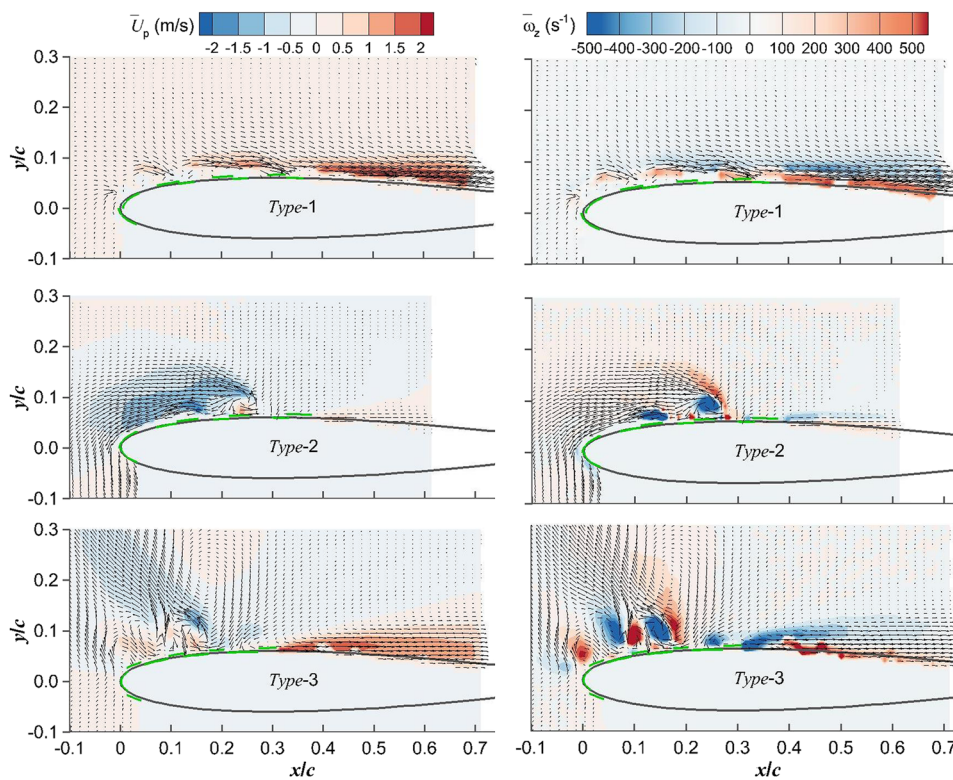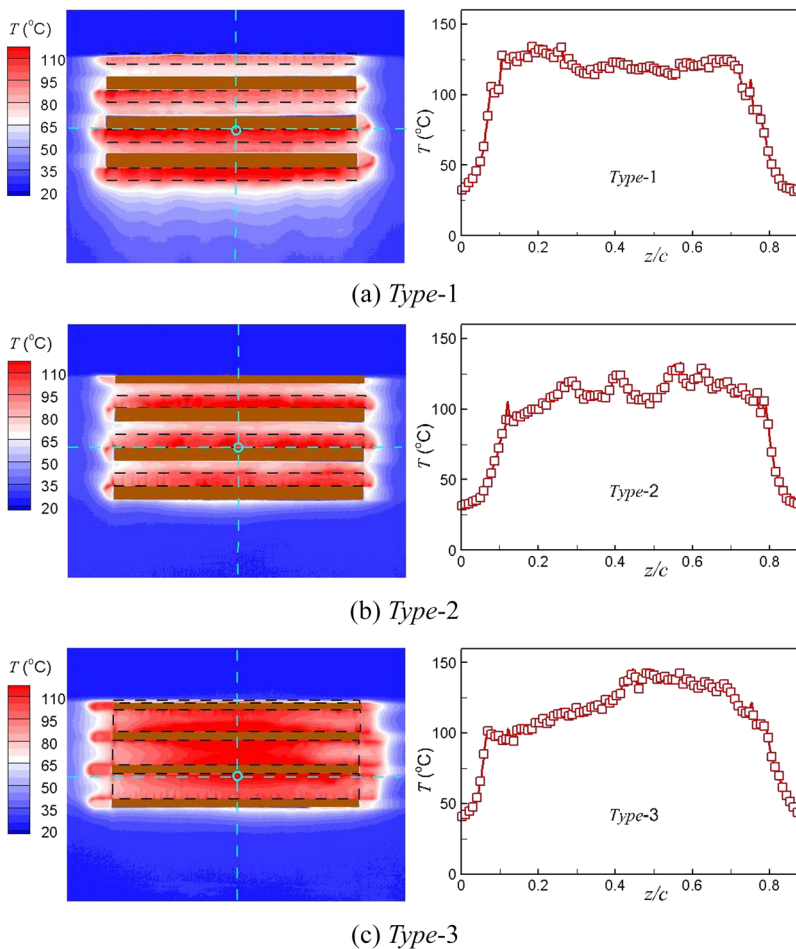

FIG. 4. Time-averaged velocity (left) and vorticity (right) induced by three different types of plasma actuators in still air.

FIG. 5. Surface temperature contours (left) and temperature distributions along the span (right) at t = 80 s time delays for three different types of plasma actuators. (a) *Type*-1. (b) *Type*-2. (c) *Type*-3.

distribution should be two dimensional in the spanwise direction. The non-uniformity of temperature distribution along the span is the result of the human error since the actuators are hand-made.

Figure 6 represents the time variation of the temperatures at sample points for different types of actuators. It shows that temperature increases rapidly for the first few seconds, but then slow approximate linear growth is observed. Since the anti-icing/de-icing process based on hot air generally lasts for a few minutes, the temperature variation rate after the rapid increase is more important for the icing control, which is 0.5 °C/s, 0.4 °C/s and 0.6 °C/s, respectively, for three types of actuators.

Figure 7 shows the chord-wise surface temperature along the sample lines indicated in Fig. 5 at 80 s time delay. It shows that for all three types of actuators, the temperature at the joint of the exposed electrode and covered electrode is the highest. The maximum temperature is 113.4 °C, 106.8 °C, and 152.1 °C, respectively. For the *Type*-1 actuator, the maximum surface temperature is located at the last electrode joint (x/c = 0.27), while it is located at the second electrode joint (x/c = 0.08) of the *Type*-2 actuator. For the *Type*-3

actuator, the temperature reaches the maximum value at the third electrode joint (x/c = 0.12).

Comparing the surface temperature distribution as shown in Fig. 7 and the induced velocity fields as shown in Fig. 4, it can be observed that thermal properties of plasma actuators are significantly coupled with induced flow field (i.e., the aerodynamic effect).

For the *Type*-1 actuator, the downstream induced flow is developed along the chord; this induced flow helped in carrying the heat from the first electrode to the last, and therefore the heat is maximized at the last electrode. The temperature drops after the actuator region for the *Type*-1 actuator are slower than the other two actuators because the induced flow for *Type*-1 is in the downward chordwise direction. For the *Type*-2 actuator, the upstream induced flow is developed along the chord, and therefore the maximum heat is observed for the electrode immediately adjacent to the leading edge.

For the *Type*-3 actuator, the discharge existing at both sides of the exposed electrodes produces a larger area of plasma, which releases more thermal energy into the surrounding air due to the induced flow. The highest surface
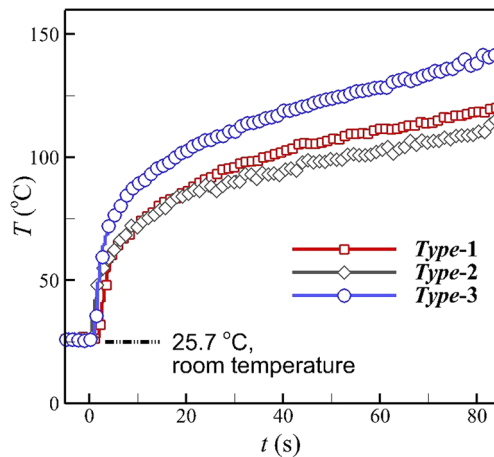
FIG. 6. Temperature variations with operation times for different types of actuators in still air.

temperature occurs in the region of maximum induced velocity and vorticity.

Coupled aerodynamic and thermal effects can affect the flow fields both inside and outside the boundary layer.[18,20–22]

It has been found that there is a direct relation between the initial ice accumulation and the boundary layer transition.[44] The actuator can control the ice accumulation by affecting the streamlines and the temperature distributions near the surface of the model, i.e., the interface between the model surface and the ice, and that of the water film and airflow.

IV. POWER CONSUMPTION

The voltage and current for all three types of actuators are measured in icing wind tunnel. The measurements are made before and after the water droplet impact and given in Figs. 8(a)–8(c) for *Type*-1, *Type*-2, and *Type*-3, respectively. The instantaneous current for positive half cycle and negative half cycle is not consistent with each other, as observed in previous studies.[45] The oscillations in instantaneous current curves show the filament discharge of the actuators.[18] It can be observed that as the water droplets are impinged on the surface of the actuators, the instantaneous voltage is reduced for all three types.

For *Type*-1 and *Type*-2, in the first half of positive semi-period, after the water droplets impact, the oscillations for the current curve are reduced, i.e., the water droplets impingement on the surface of the actuator limits the filament discharge. However, in the first half of negative semi-period, the
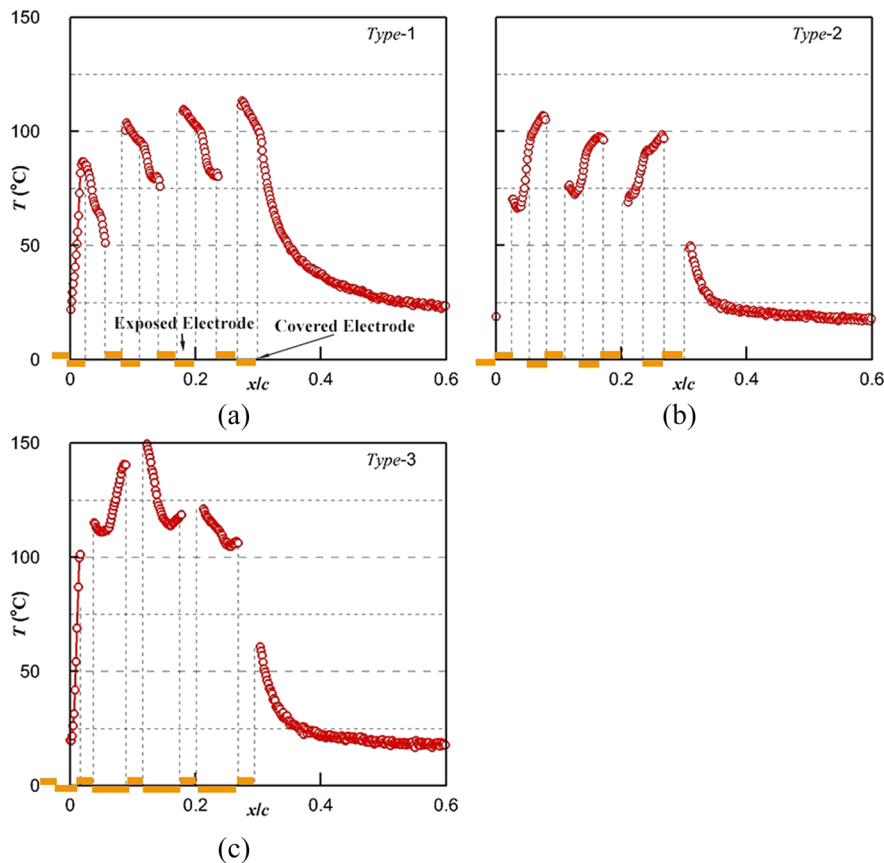
FIG. 7. Surface temperature distributions in chordwise direction for different types of actuators in still air. (a) *Type*-1. (b) *Type*-2. (c) *Type*-3.
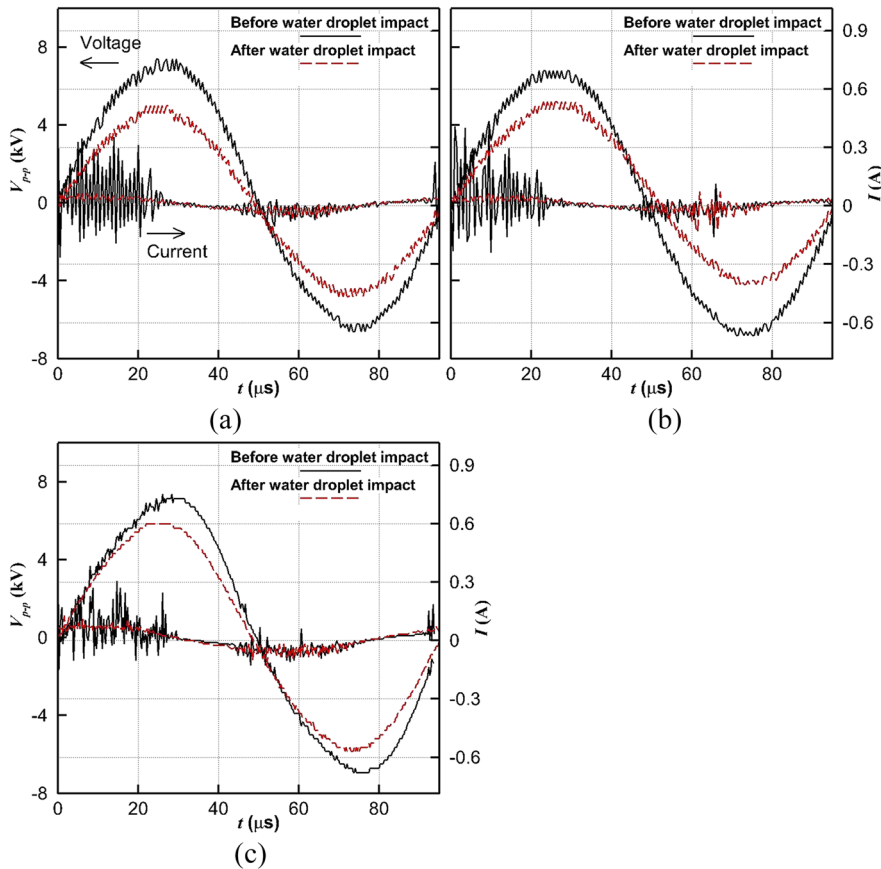
FIG. 8. Voltage and current variation with operation times for different types of actuators in icing wind tunnel for U_∞ = 40 m/s, T_∞ = −5 °C, and LWC = 1.0 g/m³. (a) $Type$-1. (b) $Type$-2. (c) $Type$-3.

amplitude for the oscillation of the current curve is basically the same as that before the water droplet impact, indicating that the impact of water droplets has almost no effect on the discharge in this phase.

For $Type$-3, in the first half of period, the oscillations of the current curve after the droplet impact are reduced, but the reduction is not significant, and it shows that for the $Type$-3 actuator, comparatively more filament discharges maintain on the surface than previous two types.

Based on measured voltage and current, the power consumption P from 0 to T seconds can be given by

$$P = \int_0^T V(t) \cdot I(t)dt,$$

where V, I, and T are voltage, current, and activation period, respectively.

The power consumption for all three types after the water droplet impact is shown in Table I. It can be seen that for

TABLE I. Power consumption for different types of actuators in icing wind tunnel for U_∞ = 40 m/s, T_∞ = −5 °C, and LWC = 1.0 g/m³.

| Actuator configuration	$Type$-1	$Type$-2	$Type$-3
P (W)	47	37	86

$Type$-1 and $Type$-2, the power consumption is 47 W and 37 W, respectively. However, for $Type$-3, considerable higher value of power is observed, i.e., 86 W. The power consumption for $Type$-3 is almost double as compared to $Type$-1 and $Type$-2.

As shown in previous studies, the power consumption and heat generation of the DBD plasma actuator are dependent upon ambient gas temperature.[29] In the present study, the ambient gas temperature in the icing wind tunnel is kept the same (−5 °C) for all the tests. Therefore, heat generated by $Type$-3 will be much higher than $Type$-1 and $Type$-2, as the power consumption for this type is higher.

V. PLASMA ICING CONTROL AND ITS MECHANISM

The ice accumulation for plasma control with a wind speed of 40 m/s and a static temperature of −5 °C is discussed in this subsection. Figure 9 shows the time evolution of the surface temperatures at six sample points, $Sp1$-$Sp4$ and $Sp1'$-$Sp2'$, which are located, respectively, on the sample lines of $Sl1$ and $Sl2$; see Fig. 3.

It can be seen that after the plasma is turned on and the water spray is turned off, the surface temperatures of the sample points on the plasma-off side are kept approximately at −5 °C, which is consistent with the static temperature of
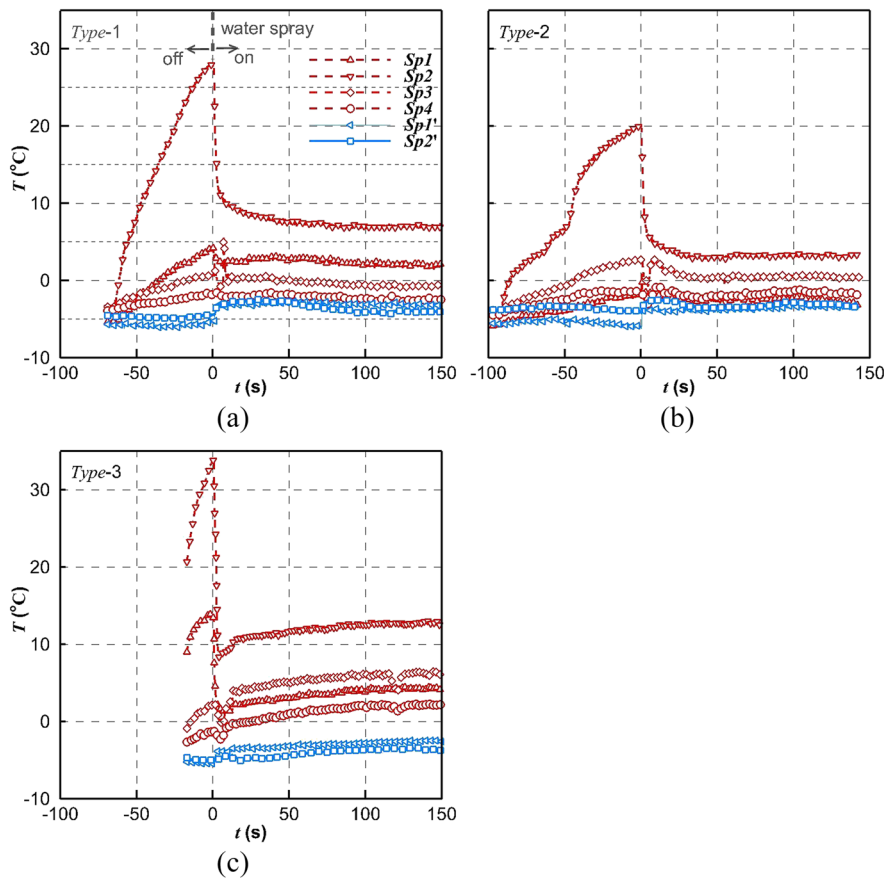
FIG. 9. Temperature variation with operation times for different types of actuators in icing wind tunnel for U_∞ = 40 m/s, T_∞ = −5 °C, and LWC = 1.0 g/m³. (a) $Type$-1. (b) $Type$-2. (c) $Type$-3.

the incoming flow. While on the plasma-on side, the surface temperature at the sample points rises gradually. The temperature variation rates of the sample points are different, while it is much smaller than that of the actuator characterization test; see Fig. 7.

The temperature at the sample points $Sp1$ and $Sp2$ is higher, as these actuators are upstream on the airfoil. Whereas, the points $Sp3$ and $Sp4$ are downstream of airfoil and comparatively lower temperature is observed on these two sample points. However, at the same locations, the surface temperature of the $Type$-3 actuator is the highest, and the temperature of the $Type$-1 actuator is greater than that of $Type$-2.

After the spraying (i.e., water spray turned on), on the plasma-off side, the temperatures of the sample points $Sp1'$ and $Sp2'$ were slightly increased, which is more dominant for the actuators of $Type$-1 and $Type$-2. At the sample point $Sp1'$ (closer to the leading edge), the temperature jump is about 2 °C. At the sample point $Sp2'$, it is about 1.5 °C. This phenomenon is due to the accumulation of the latent heat of fusion with the continuous impingement of the super-cooled water droplets onto the airfoil surface.[46] The greater temperature rise of the sample point $Sp1'$ is due to more impingements of the super-cooled water droplets at the leading edge.

On the plasma-on side, the temperature of sample points $Sp1$ and $Sp2$ drops sharply for the early few seconds due to the rapid cooling associated with super-cooled droplet impingement. At all the sample points, the surface temperatures become stable at about t = 100 s, which means the heat of the plasma discharge would eventually reach a balanced state, and heat dissipation of the super-cooled water droplets balances with the surrounding air. Therefore, we take the results of t = 112 s as the final icing control results using plasma actuation.

Figure 10 shows the snapshots of the instantaneous images at t = 112 s time delay to visualize the ice accumulation after the thermal equilibrium. On the plasma-off side for all three types of actuators, there is a clear glaze ice accumulation from the leading edge to 37% c, which is the direct impacting region of the super-cooled water droplets. The maximum icing thickness appears at the leading edge, which is about 3% c (4 mm).

On the plasma-on side, the different ice accumulations occur for the different types of actuators. For the $Type$-1 actuator, the plasma actuation ensures that there is no ice on the leading edge of the airfoil, and the ice accumulation appears at approximately 57% c of the model. While for the $Type$-2 actuator, there is a little ice accumulation on the leading edge,
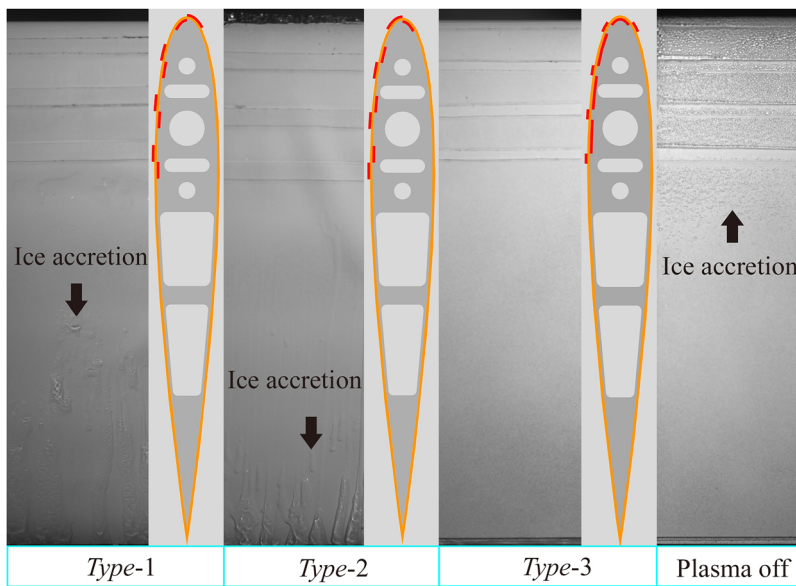
FIG. 10. Ice accumulation for U_∞ = 40 m/s, T_∞ = −5 °C, and LWC = 1.0 g/m³ at t = 112 s.

but the ice accumulation is delayed to 81% c. With the same test conditions, the $Type$-3 actuator significantly prevented the appearance of the solid ice over the entire lower surface of the airfoil.

Figure 11 demonstrates the temperature contours on the lower surface of the airfoil corresponding to Fig. 10. On the plasma-off side, the surface temperature is −4 °C for most of the region. On the plasma-on side, the surface temperatures in the region of attached actuators are always well above 0 °C for all types of the actuators. The highest measured temperature is 20.3 °C, 11.5 °C, and 20.8 °C for $Type$-1, $Type$-2, and $Type$-3 actuators, respectively. The highest temperatures of $Type$-2 and $Type$-3 actuators appear at the joints between

the exposed and covered electrodes, while that of the $Type$-1 actuator appears above the covered electrodes.

$Type$-1 and $Type$-2 actuators have the same number and area of electrodes. The input power for these two actuators is also the same; therefore, the heat generated by plasma discharge is the same. However, the IR camera measurements show that the airfoil surface temperature is significantly different after reaching the thermal equilibrium, so it can be inferred that the induced flow field of the actuator plays a vital role in the anti-icing experiment. Different induced airflows have different effects on the mixing between discharge heat and incoming flow, resulting in different anti-icing effects.
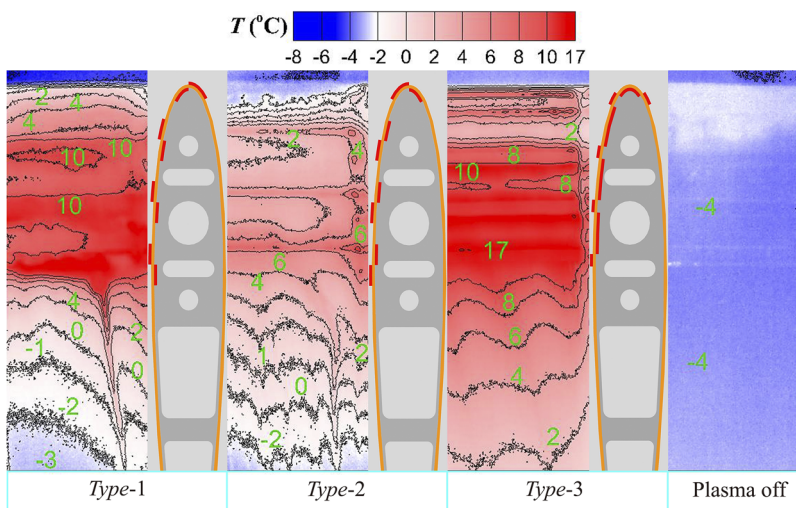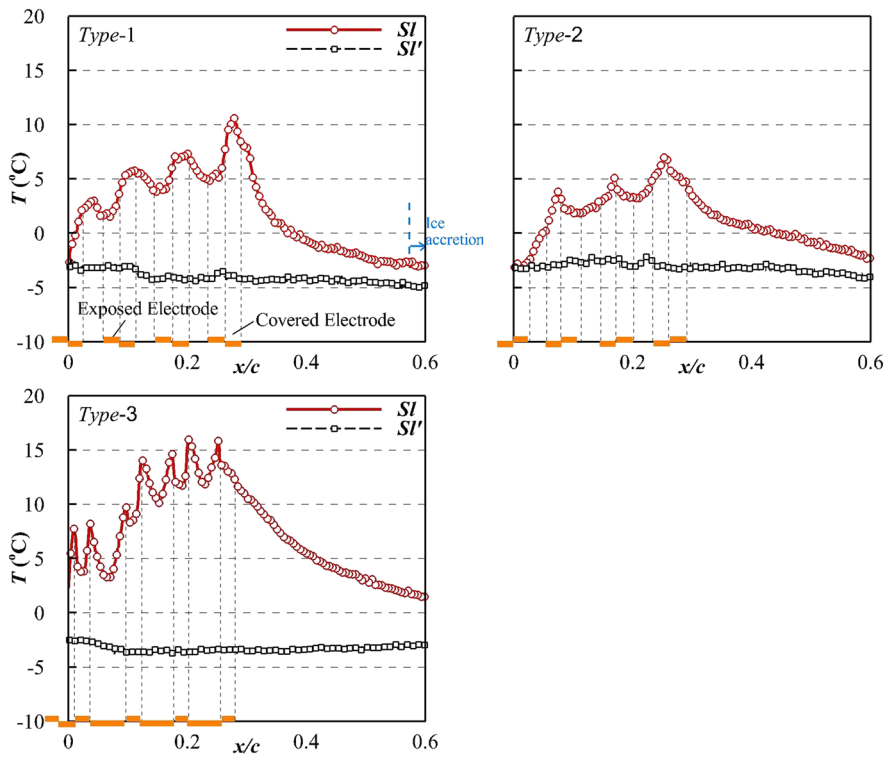

FIG. 11. Surface temperature of ice accumulation for U_∞ = 40 m/s, T_∞ = −5 °C, and LWC = 1.0 g/m³ at t = 112 s.

FIG. 12. Temperature distributions along Sl and Sl' sample lines at t = 112 s for U_∞ = 40 m/s, T_∞ = −5 °C, and LWC = 1.0 g/m^3.

Figure 12 shows the temperature distributions on two sample lines, Sl and Sl', which are located chordwise on plasma-on and plasma-off sides, respectively. The Sl sample line shows an increasing oscillatory behavior along the chord of the actuator. It means that the water film is heated by the series of the single plasma electrode. The Sl' sample line is almost a straight line. It shows the surface temperature on the plasma-off side becomes stable after the thermal equilibrium.

Comparing Type-1 in Figs. 10–12, it can be seen that the temperature corresponding to the icing is about −3 °C. This is because the surface of the airfoil is covered by water film, and in the presence of incoming flow, the water film and incoming flow will interact with each other causing the freezing point to be below 0 °C.[47]

The ice accumulation process with plasma actuation can be explained using Figs. 10–12. During the experiment, the plasma actuator generates heat on activation. The supercooled water droplets impinging on the actuator would be heated. As the heat generated by the plasma actuator is not enough to directly vaporize these water droplets, they will exist in the form of liquid water and form a water film on the surface of the airfoil with the incoming flow. The water film flows over the airfoil surface and forms multiple finger-like rivulet structures in the further downstream region. For different types of actuators, the finger-like water film exhibited different developments after the thermal equilibrium.

For the $Type$-3 actuator, the heat generated by the actuator is sufficient to prevent the water film from freezing on the entire lower surface of the airfoil. The water is collecting at the trailing edge and finally flies away with the surface airflow. Thus, no ice is found on the plasma-on side. While for the $Type$-1 and $Type$-2 actuators, such heat is not enough, so the ice accumulation occurs at, respectively, 57% and 81% chord of the lower surface of the airfoil, as shown in Fig. 10.

Comparing the results of the plasma actuator characterization and the wind tunnel test, Fig. 13 presents a schematic diagram of the plasma icing control based on thermal and aerodynamic coupling effects. The mechanism of the different effects of icing control caused by the different types of the plasma actuators is discussed here.
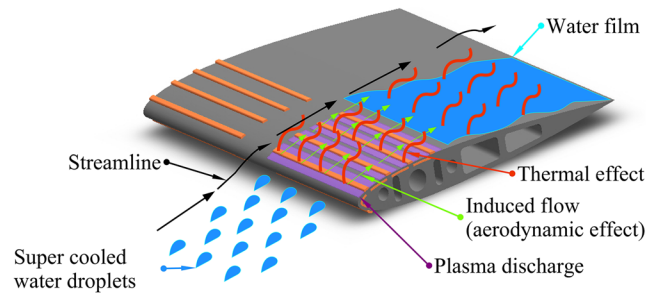
FIG. 13. Mechanism illustration of plasma icing control.

It is known from the actuator characterization test that the plasma actuation produces both the heat and the induced airflow. The plasma discharge heat is the most direct cause of plasma icing control. The induced velocity mixing with the incoming flow can effectively affect the heat transfer. In this experiment, because of the presence of water film, the effect of the induced airflow on heat transfer is reflected in the downstream transfer efficiency of the heat carried by the water film and the surface airflow. This conclusion can be demonstrated by the different anti-icing effects of the three types of plasma actuators.

For the *Type*-1 actuator, the induced airflow produced is consistent with the direction of the incoming flow so that it is very close to the wall. The induced airflow close to the wall is not capable of transferring more heat to the farther downstream due to the boundary layer. That is the reason that the effective ice protection area of the *Type*-1 actuator is smaller than the other two types of actuators.

The induced airflow generated by the *Type*-2 actuator is opposite to the incoming flow, so the heat it carries is being better mixed with the incoming flow than the *Type*-1 actuator; therefore, this heat can be transmitted to a farther distance. The different coupled induced airflow and heat effects cause the different anti-icing results for *Type*-1 and *Type*-2 actuators. For the *Type*-2 actuator, the temperature over the plasma region is lower than that of the *Type*-1 actuator, but the ice accumulation is closer to the trailing edge and is delayed by 24% c in comparison with the *Type*-1 actuator. For the *Type*-3 actuator, the discharge existing at both sides of the exposed electrodes produces more thermal energy, so the temperature of the local surface is higher than the other two actuators. Its higher induced airflow and the corresponding vorticity can supply the most effective convective heat transfer, which transferred more heat downstream, ensuring that the entire airfoil surface is free of icing accumulation.

VI. CONCLUSIONS

Plasma actuation is feasible and effective for in-flight anti-icing, and it has the potential to meet the icing control needs of next-generation aircraft. Three types of actuators have been designed to generate the induced flows in different directions. The actuators have been characterized in still air at atmospheric pressure. Through detailed PIV and surface temperature measurements, the present experimental study confirms that the plasma discharge heat is coupled with the induced velocity and the corresponding vorticity.

The results in an icing wind tunnel show that the anti-icing performance is directly related to the design of the plasma actuators based on the coupled aerodynamic and thermal effects. When the induced flow field of the actuator is consistent with the incoming flow although the local temperature is higher, the surface ice accumulation is more upward, i.e., toward leading edge; when the induced flow field is opposite to the incoming flow, the local surface temperature of the actuator is lower, and the ice accumulation is more downward, i.e., toward trailing edge. Such a result is the direct evidence

of the following mechanism: when the induced velocity is consistent with the incoming flow, the effect of induced velocity is near the wall which helps the coupled heat effect to stay close to the wall, the near wall effect opposes the mixing of incoming flow and heat effect. For the opposite induced velocity, the plasma-induced flow has an obvious influence on the leading edge, the opposite induced velocity favours the heat mixing; therefore, the coupling heat is mixed easily and carried further.

When the actuator induces the flow velocity approximately perpendicular to the incoming flow, the actuator has a higher local temperature and there is no icing on the entire lower surface of the airfoil. It implies that the actuator can generate more heat and this heat is transferred more effectively with the incoming flow. Therefore, the criterion for plasma actuator optimization for anti-icing is that the actuator can generate as much heat as possible locally, and at the same time, it should be easily carried by the induced flow and better mixed with the incoming flow.

Although this study clearly demonstrates that plasma anti-icing effects are directly related to coupled thermal and aerodynamic effects of plasma actuators, but still further research is required for the detailed and insightful cause-and-effect relationship between the plasma discharge and the icing. In the present study, the spatially induced velocity distribution of the plasma is measured only in the quiescent air, and the discharge thermal effect is measured by the temperature distribution on the surface of the actuators. The most important part of future work is to establish a direct connection between the plasma aerodynamic effect and the thermal effect based on experimental research or numerical simulation. Furthermore, the effects of plasma actuation (both thermal and aerodynamic effects) on the flow around the airfoil in the icing environment should be studied, and the changes in the spatial velocity field and the surface pressure field with plasma actuation should be studied in detail in future work.

In addition, the more efficient mixing of the plasma-induced heat and incoming flow is related to the aerodynamic characteristics of the airfoil itself, which includes parameters like the angle of attack, Mach number, and Reynolds number. The effect of these parameters on plasma icing control needs to be studied in future work. Furthermore, as mentioned in Sec. I, a great advantage of the plasma icing control system is that it can be integrated with the plasma flow control system in non-icing environments. Therefore, when designing an actuator based on coupled aerodynamic and thermal effects, a positive effect on flow control is also need to be considered.

REFERENCES

[1] R. W. Gent, N. P. Dart, and J. T. Cansdale, "Aircraft icing," Philos. Trans. R. Soc., A **358**, 2873 (2000).

[2] T. Cebeci and F. Kafyeke, "Aircraft icing," Annu. Rev. Fluid Mech. **35**, 11–21 (2003).

[3] K. R. Petty and C. D. J. Floyd, "A statistical review of aviation airframe icing accidents in the US," in *Proceedings of the 11th Conference on Aviation, Range, and Aerospace, Hyannis, MA, 4-8 October 2004* (American Meteorological Society, 2004).

[4] O. Parent and A. Ilinca, "Anti-icing and de-icing techniques for wind turbines: Critical review," Cold Reg. Sci. Technol. **65**, 88–96 (2011).

[5] Z. A. Janjua, B. Turnbull, S. Hibberd, and K.-S. Choi, "Mixed ice accretion on aircraft wings," Phys. Fluids **30**, 027101 (2018).

[6] M. Pourbagian, B. Talgorn, W. Habashi, M. Kokkolaras, and S. L. Digabel, "Constrained problem formulations for power optimization of aircraft electro-thermal anti-icing systems," Optim. Eng. **16**, 663–693 (2015).

[7] S. K. Thomas, R. P. Cassoni, and C. D. MacArthur, "Aircraft anti-icing and de-icing techniques and modeling," J. Aircr. **33**, 841–854 (1996).

[8] W. Dong, J. Zhu, M. Zheng, and Y. Chen, "Thermal analysis and testing of nonrotating cone with hot-air anti-icing system," J. Propul. Power **31**, 896–903 (2015).

[9] A. Abbas, J. de Vicenteb, and E. Valerob, "Aerodynamic technologies to improve aircraft performance," Aerosp. Sci. Technol. **28**, 100–132 (2013).

[10] T. G. Myers, J. P. Charpin, and S. J. Chapman, "The flow and solidification of a thin fluid film on an arbitrary three-dimensional surface," Phys. Fluids **14**, 2788–2803 (2002).

[11] N. Chen, H. Ji, G. Cao, and Y. Hu, "A three-dimensional mathematical model for simulating ice accretion on helicopter rotors," Phys. Fluids **30**, 083602 (2018).

[12] A. Lampton and J. Valasek, "Prediction of icing effects on the lateral/directional stability and control of light airplanes," Aerosp. Sci. Technol. **23**, 305–311 (2012).

[13] A. Shinkafi and C. Lawson, "Enhanced method of conceptual sizing of aircraft electro-thermal de-icing system," Int. J. Aerosp. Mech. Eng. **8**, 1073–1080 (2014).

[14] P. C. E. Harris, "Opportunities for next generation aircraft: Enabled by revolutionary materials," in *AIAA SDM Conference* (AIAA, 2011).

[15] A. Carlo, I. Massimiliano, H. Tobias, M. Marco, and A. Alidad, "Understanding the effect of superhydrophobic coatings on energy reduction in anti-icing systems," Cold Reg. Sci. Technol. **67**, 58–67 (2011).

[16] M. Miwa, A. Nakajima, A. Fujishima, K. Hashimoto, and T. Watanabe, "Effects of the surface roughness on sliding angles of water droplets on superhydrophobic surfaces," Langmuir **16**, 5754–5760 (2000).

[17] N. Nagappan, V. V. Golubev, and W. Habashi, "Parametric analysis of icing control using synthetic jet actuators," AIAA Paper 2013-2453, 2013.

[18] E. Moreau, "Airflow control by non-thermal plasma actuators," J. Phys. D: Appl. Phys. **40**, 605–636 (2007).

[19] T. N. Jukes and K.-S. Choi, "Flow control around a circular cylinder using pulsed dielectric barrier discharge surface plasma," Phys. Fluids **21**, 084103 (2009).

[20] J. Little and M. Samimy, "High-lift airfoil separation with dielectric barrier discharge plasma actuation," AIAA J. **48**, 2884–2898 (2010).

[21] B. E. Mertz and T. C. Corke, "Single-dielectric barrier discharge plasma actuator modelling and validation," J. Fluid Mech. **669**, 557–583 (2011).

[22] J. Wang, K. S. Choi, L. Feng, T. Jukes, and R. D. Whalley, "Recent developments in DBD plasma flow control," Prog. Aerosp. Sci. **62**, 52–78 (2013).

[23] L. Shen, C.-Y. Wen, and H.-A. Chen, "Asymmetric flow control on a delta wing with dielectric barrier discharge actuators," AIAA J. **54**, 652–658 (2015).

[24] X. Meng, Y. Long, J. Wang, F. Liu, and S. Luo, "Dynamics and control of the vortex flow behind a slender conical forebody by a pair of plasma actuators," Phys. Fluids **30**, 024101 (2018).

[25] N. L. Aleksandrov, S. V. Kindysheva, M. M. Nudnova, and A. Y. Starikovskiy, "Mechanism of ultra-fast heating in a non-equilibrium weakly ionized air discharge plasma in high electric fields," J. Phys. D: Appl. Phys. **43**, 255201 (2010).

[26] S. A. Stanfield, J. Menart, C. DeJoseph, Jr., R. L. Kimme, and J. R. Hayes, "Rotational and vibrational temperatures for a dielectric barrier discharge in air using emission spectroscopy," AIAA Paper 2007-3876, 2007.

[27] B. Dong, J. M. Bauchire, J. M. Pouvesle, P. Magnier, and D. Hong, "Experimental study of a DBD surface discharge for the active flow control of subsonic airflow," J. Phys. D: Appl. Phys. **41**, 155201 (2008).

[28] R. Joussot, D. Hong, H. Rabat, V. Boucinha, R. Weber-Rozenbaum, and A. L. Chesneau, "Thermal characterization of a DBD plasma actuator: Dielectric temperature measurements using infrared thermography," AIAA Paper 2010-5102, 2010.

[29] R. Erfani, H. Z. Behtash, and K. Kontis, "Plasma actuator: Influence of dielectric surface temperature," Exp. Therm. Fluid Sci. **42**, 258–264 (2012).

[30] T. Rakshit, B. Nicolas, M. Eric, F. Matthieu, L. Gildas, and D. Eva, "Temperature characterization of dielectric barrier discharge actuators: Influence of electrical and geometric parameters," J. Phys. D: Appl. Phys. **47**, 255203 (2014).

[31] F. Rodrigues, J. Pascoa, and M. Trancossi, "Heat generation mechanisms of DBD plasma actuators," Exp. Therm. Fluid Sci. **90**, 55–65 (2018).

[32] F. Rodrigues, J. Pascoa, and M. Trancossi, "Experimental analysis of dielectric barrier discharge plasma actuators thermal characteristics under external flow influence," J. Heat Transf. **140**(10), 102801 (2018).

[33] X. Meng, Z. Chen, and K. Song, "AC- and NS-DBD plasma flow control research," in *Proceedings of the 2nd NPU-DLR Workshop on Aerodynamics* (DLR, Institut für Aerodynamik und Strömungstechnik, 2014), pp. 1–75, DLR-IB 124-2014/5.

[34] X. Meng, J. Cai, Y. Tian, X. Han, and D. Zhang, "Experimental study of anti-icing and deicing on a cylinder by DBD plasma actuation," AIAA Paper 2016-4019, 2016.

[35] J. Cai, Y. Tian, X. Meng, X. Han, D. Zhang, and H. Hu, "An experimental study of icing control using DBD plasma actuator," Exp. Fluids **58**, 102 (2017).

[36] S. G. Pouryoussefi, M. Mirzaei, F. Alinejad, and S. M. Pouryoussefi, "Experimental investigation of separation bubble control on an iced airfoil using plasma actuator," Appl. Therm. Eng. **100**, 1334–1341 (2016).

[37] W. Zhou, Y. Liu, H. Hu, H. Hu, and X. Meng, "Utilization of thermal effect induced by plasma generation for aircraft icing mitigation," AIAA J. **56**, 1097–1104 (2018).

[38] Y. Tian, Z. Zhang, J. Cai, L. Yang, and L. Kang, "Experimental study of an anti-icing method over an airfoil based on pulsed dielectric barrier discharge plasma," Chin. J. Aeronaut. **31**, 1449–1460 (2018).

[39] C. Zhang and H. Liu, "Effect of drop size on the impact thermodynamics for supercooled large droplet in aircraft icing," Phys. Fluids **28**, 062107 (2016).

[40] T. Okada, R. Ishige, and S. Ando, "Analysis of thermal radiation properties of polyimide and polymeric materials based on ATR-IR spectroscopy," J. Photopolym. Sci. Technol. **29**, 251–254 (2016).

[41] R. Ely and J. Little, "Mixing layer excitation by dielectric barrier discharge plasma actuators," AIAA Paper 2013-2753, 2013.

[42] S. Grundmann and C. Tropea, "Experimental transition delay using glow discharge plasma actuators," Exp. Fluids **42**, 653–657 (2007).

[43] X. Meng, H. Hu, X. Yan, F. Liu, and S. Luo, "Lift improvements using duty-cycled plasma actuation at low Reynolds numbers," Aerosp. Sci. Technol. **72**, 123–133 (2018).

[44] R. J. Hansman, K. Yamaguchi, B. Berkowitz, and M. Potapczuk, "Modeling of surface roughness effects on glaze ice accretion," J. Thermophys. Heat Transfer **5**, 54–60 (1991).

[45] C. Enloe, T. E. McLaughlin, R. D. Van Dyken, K. Kachner, E. J. Jumper, and T. C. Corke, "Mechanisms and responses of a single dielectric barrier plasma actuator: Plasma morphology," AIAA J. **42**, 589–594 (2004).

[46] R. J. Hansman and S. R. Turnock, "Investigation of surface water behavior during glaze ice accretion," J. Aircr. **26**, 140–147 (1989).

[47] B. L. Messinger, "Equilibrium temperature of an unheated icing surface as a function of air speed," J. Aeronaut. Sci. **20**, 29–42 (1953).